Electronic structure of $Ce_nM_mIn_{2m+3n}$, where $n = 1, 2$; $m = 0, 1$;M = Co, Rh or Ir: experiment and calculations

2008 J. Phys.: Condens. Matter 20 115202

(http://iopscience.iop.org/0953-8984/20/11/115202)

J. Phys.: Condens. Matter **20** (2008) 115202 (17pp) doi:10.1088/0953-8984/20/11/115202

Electronic structure of $Ce_nM_mIn_{2m+3n}$, where $n = 1, 2$; $m = 0, 1$; M = Co, Rh or Ir: experiment and calculations

M Gamża[1], A Ślebarski[1] and J Deniszczyk[2]

[1] Institute of Physics, University of Silesia, 40-007 Katowice, Poland
[2] Institute of Materials Science, University of Silesia, 40-007 Katowice, Poland

Received 21 September 2007, in final form 11 January 2008
Published 20 February 2008
Online at stacks.iop.org/JPhysCM/20/115202

Abstract

We present a detailed study of the electronic structure of the $Ce_nM_mIn_{2m+3n}$ (M = Co, Rh, Ir; $n = 1, 2$ and $m = 0, 1$) series of Ce intermetallic compounds and of the reference $LaIn_3$ compound. The ground state of these heavy-fermion (HF) materials can be tuned between antiferromagnetic (AF) and superconducting (SC), with pressure or doping as the tuning parameter. Performing the x-ray photoelectron spectroscopy (XPS) measurements on the Ce 3d core levels as well as on the valence band states we analyse the dependence of both the Ce 4f band character and physical properties on the kind of transition metal atom M and on the number of $CeIn_3$ layers intervened by the MIn_2 layers in the investigated family of compounds. We draw a parallel between the XPS valence band spectra and *ab initio* band structure calculations based on the full-potential linearized augmented plane-wave (FP-LAPW) method. We analyse changes in valence band states within the whole family of materials. We compare the experimental magnetic moments on Ce atoms with the theoretical ones calculated within different approximations for exchange–correlation potential. Finally, we have shown that the Ce 4f electrons participate in bonding formation for all investigated compounds. Our study indicates that the observed changes in the 4f band on-site hybridization energy result from the reconstruction of the charge density distribution driven by transition metal atoms inserted into the $CeIn_3$ structure.

(Some figures in this article are in colour only in the electronic version)

1. Introduction

In recent years, the investigations of Ce-based systems, where the long-range Ruderman–Kittel–Kasuya–Yoshida (RKKY) interaction and the local on-site exchange interaction (Kondo effect) compete with each other, have attracted much attention. If the RKKY interaction predominates, various magnetic ground states can occur [1]. Otherwise, the hybridization between the localized f electron and the conduction states can lead to formation of a heavy-fermion (HF) liquid [2]. An especially intriguing situation occurs near a magnetic instability, i.e., close to the phase transition between magnetically ordered and non-magnetic ground states. The most interesting are HF systems, in which superconductivity (SC) appears near the boundary between the magnetic and non-magnetic states, suggesting that magnetic interactions may play an essential role in the formation of the Cooper pairs in the SC state.

The $Ce_nM_mIn_{2m+3n}$ materials are examples of such behaviour. It is visible in the (T, P) phase diagram of the parent compound $CeIn_3$ [3–5], which exhibits AF with $T_N = 10.2$ K at atmospheric pressure. With applied pressure, T_N decreases and SC occurs with a maximum value of $T_C \sim 0.2$ K found in a narrow P-range around $P_c \sim 2.6$ GPa, where $T_N \to 0$. Likewise $CeRhIn_5$, ordered antiferromagnetically below $T_N = 3.8$ K, exhibits a transition to the superconducting state with T_C of 2.2 K at the pressure of 2.5 GPa [6–9]. The microscopic coexistence of AF and SC has been found in a range of pressure of 1.53–1.9 GPa, whereas $CeCoIn_5$ and $CeIrIn_5$ are HF superconductors at atmospheric pressure with T_C values of 2.3 K and 0.4 K, respectively [10, 11]. Similar properties characterize the Ce_2MIn_8 subfamily. Namely, Ce_2CoIn_8 is an HF superconductor with $T_C \sim 0.4$ K [12]; Ce_2RhIn_8 exhibits AF with $T_N \sim 2.8$ K at atmospheric pressure and transition to the superconducting state with rising

pressure, showing $T_C \sim 2$ K at the pressure of 2.25 GPa [7, 13]. Ce_2IrIn_8 is an HF paramagnet down to 50 mK [7].

The parent $CeIn_3$ system forms in a simple cubic $AuCu_3$-type structure [14]. The compounds with transition metal atoms M crystallize in the quasi-two-dimensional (quasi-2D) tetragonal structures Ho_nCoGa_{2n+3} [15], that can be viewed as n layers of $CeIn_3$ units stacked sequentially along the c-axis with intervening m layers of MIn_2. Therefore, the $Ce_nM_mIn_{2m+3n}$ systems gave us a unique opportunity for investigation of the influence of systematic structure modifications on both electronic structure and physical properties of these compounds. On the one hand we can investigate the changes arising from the gain in the number of $CeIn_3$ layers intervened by the MIn_2 layers, and on the other hand we can analyse the dependence on the kind of transition metal atom in the series of Ce_2MIn_8 and $CeMIn_5$ compounds.

An especially important question, which is worth studying, is the role of the 4f electrons and their degree of localization in formation of the unconventional ground states. Although many advances have been achieved in explanation of the electronic structure, especially within the $CeMIn_5$ subfamily [5, 16–26], the character of the Ce 4f electrons in these materials is still somewhat controversial. For instance, for AF $CeRhIn_5$ a nuclear quadrupole resonance (^{115}In NQR) study revealed the strong hybridization of the 4f electrons with the conduction band in a very low temperature region and localized character of 4f states at higher temperatures (above ∼10 K) [5, 17]. On the other hand, Moore *et al* interpreted the results of the angle-resolved photoelectron spectroscopy (ARPES) within the framework of an itinerant 4f electron model [18]. Meanwhile, the combined ARPES, the Ce 3d–4f resonant photoemission spectroscopy (RPES) and the x-ray absorption spectroscopy (XAS) experiments [19] suggested a relatively localized character of the Ce 4f states at temperature ∼ 15 K, in agreement with results from the NQR experiment. Besides, some de Haas–van Alphen (dHvA) experiments were interpreted within the itinerant 4f electron picture [20], while the following detailed dHvA study showed that in $CeRhIn_5$ the Ce 4f states do not contribute to the volume of the Fermi surface [21, 22, 27].

For SC $CeIrIn_5$, as for $CeCoIn_5$, the topology and size of the Fermi surface investigated by the dHvA effect suggest the itinerant character of the 4f electron [20, 22, 23, 27]. In addition, NQR study confirmed that 4f electrons in $CeIrIn_5$ are much more itinerant than in the other known Ce-based HF compounds [24]. In contrast, some photoemission experiments (ARPES and Ce 3d–4f RPES) showed that in this compound Ce 4f states are nearly localized [19]. Finally, recent Ce 3d–4f RPES investigations for $CeIrIn_5$ revealed [25] that, although the Ce 4f spectra are dominated by the localized character, there is also a small itinerant contribution originating from the hybridization, observed as the quasi-particle band near ϵ_F. This is consistent with a very high value of Sommerfeld coefficient of 750 mJ (mol $K^2)^{-1}$ [11].

In contrast, for parent AF compound $CeIn_3$ different experimental data gave evidence for a strongly bound character of the Ce 4f states at ambient pressure [28–30]. However, the large value of specific heat coefficient of 130 mJ (mol $K^2)^{-1}$ [3] indicates that there is some contribution of the 4f states at the Fermi level.

We performed the x-ray photoelectron spectroscopy (XPS) measurements for the family of $Ce_nM_mIn_{2m+3n}$ compounds to investigate the changes in hybridization between Ce 4f states and the conduction band resulting either from the M-element substitution or the number of $CeIn_3$ layers intervened by the MIn_2 layers. Based on the Ce 3d XPS spectra we also discuss the valence of Ce ions. We analyse the XPS valence band spectra in the context of *ab initio* band structure calculations. To get more precise information about the Ce 4f bands in $CeIn_3$ we combined the XPS valence band spectrum of $CeIn_3$ with that of the isostructural reference $LaIn_3$ compound. We also carried out band structure calculations using the full-potential local-orbital minimum-basis (FPLO) code [32] to clarify the contributions to the valence band originating from states of Ce and In with different l-symmetry extended into the interstitial regions. The LAPW method demands the presence of the electrons in the interstitial region, which cannot be taken straightforwardly into account in a simulation of the theoretical XPS spectra, whereas the FPLO crystal potential does not introduce the interstitial regions. The compounds $CeIn_3$, $CeRhIn_5$ and Ce_2RhIn_8 have AF ground states, therefore we performed additional band structure calculations assuming antiferromagnetic alignment of Ce magnetic moments inside $CeIn_3$ layers. We investigated the influence of such magnetic order on values of the total magnetic moments as well as on the DOS near the Fermi level in both GGA and GGA + U approximations.

Finally, based on our results we analysed the changes in valence band states within the whole family of $Ce_nM_mIn_{2m+3n}$ compounds. We tried to clarify which interactions have the dominant influence on both the Ce 4f band character and the ground state properties of the investigated compounds.

2. Computational methods

The electronic structure of all compounds was studied by the full-potential linearized augmented plane-wave (FP-LAPW) method [31] using WIEN2k computer code [33]. In this method the unit cell is divided into non-overlapping muffin-tin spheres (centred at the atomic sites) and an interstitial region. The muffin-tin radii were assumed to be 2.55 au for Ce and La, 2.45 au for Co, Rh and In and 2.5 au for Ir. Inside the atomic spheres, partial waves were expanded up to $l_{max} = 10$, while the number of plane waves in the interstitial region was limited by the cut-off at $K_{max} = 8.0/R_{MT}$, where R_{MT} is the smallest of all atomic sphere radii in each system. The charge density was Fourier expanded up to $G_{max} = 14$. The calculations were spin polarized. The **k**-space integrations were done using over 330 **k** points in the irreducible wedge of the Brillouin zone (5000 points in the full zone) for $CeMIn_5$, over 260 **k** points (4000 points in the full zone) for $CeMIn_8$ and over 330 **k** points in the irreducible wedge (10 000 points in the full zone) for $CeIn_3$ and $LaIn_3$. In the AF calculations for $CeIn_3$, $CeRhIn_5$ and Ce_2RhIn_8 a similar density of **k**-mesh was assumed. Exchange–correlation (XC) effects were treated within the GGA approximation in the form proposed

by Perdew, Burke and Ernzerhof (GGA96) [34]. The following states were considered as valence: Ce (4f, 5d, 6s, 6p), La (5d, 6s, 6p), Co (3d, 4s, 4p), Rh (4d, 5s, 5p), Ir (5d, 5f, 6s, 6p) and In (5s, 5p, 5d). As semicore states we chose Ce (4d, 5s, 5p), La (4d, 5s, 5p), Co (3s, 3p), Rh (4s, 4p), Ir (4f, 5s, 5p) and In (4s, 4p, 4d). The core levels were treated fully relativistically, while for valence states relativistic effects were included in a scalar-relativistic manner [35]. Spin–orbit (SO) coupling was included in the second variational method using the scalar-relativistic eigenfunctions as basis [36]. For $CeIn_3$ the easy magnetization axis was assumed along the [111] direction, in agreement with experimental data [14], whereas for $CeMIn_5$ and Ce_2MIn_8 the [001] axis was chosen. Because the considered compounds are strongly correlated systems, we went beyond the standard GGA approximation and included the orbital dependent potentials for the Ce 4f states, applying the so called GGA + U method, introduced by Anisimov *et al* [37], with an approximate correction for the self-interaction. The exchange constant J for the Ce 4f states was assumed to be ∼1 eV. The effective U_{eff} is defined as $U_{\mathrm{eff}} = U - J$, where U is the Coulomb correlation parameter for the specified shell.

The electronic structure of $CeIn_3$ and $LaIn_3$ was also studied by the full-potential local-orbital (FPLO) minimum-basis method [32] within the local spin density approximation (LSDA) as well as using the LSDA + U approach for the Hubbard correlation interactions within the Ce 4f shell [38]. In the scalar-relativistic calculations the XC potential of Perdew and Wang was used [39]. As the basis set, Ce(4f, 5s, 5p, 5d, 6s, 6p), La(5s, 5p, 5d, 6s, 6p) and In(4s, 4p, 4d, 5s, 5p, 5d) states were employed. The lower-lying states were treated fully relativistically as core states. The In 5d states were taken into account as polarization states to increase the completeness of the basis set. The spatial extension of the basis orbitals, controlled by the confining potential exponent equal to 4, was optimized to minimize the total energy [40]. A **k**-mesh of 286 points in the irreducible part of Brillouin zone (8000 in the full zone) was used.

The electronic structures of all considered systems were computed using the experimental atomic positions and lattice parameters listed in tables 1 and 2, respectively.

Based on band structure results we calculated the theoretical XPS valence band spectra. The densities of states were convoluted by the Lorentzians with a full width at half maximum (FWHM) of 0.4 eV to account for the instrumental resolution, thermal broadening and the effect of the lifetime of the hole states. The partial l-resolved densities of states were multiplied by the corresponding cross-sections [41] and by the Fermi–Dirac function with $T = 300$ K.

3. Experimental details

Polycrystalline samples of $CeIn_3$, $LaIn_3$, $CeRhIn_5$, $CeIrIn_5$ and Ce_2RhIn_8 were prepared by arc melting stoichiometric amounts of the elemental metals (Ce 99.99%, La 99.99%, Rh 99.9%, Ir 99.99%, In 99.995%, in units of atomic%) on a water cooled cooper hearth in an ultra-high purity Ar atmosphere with an Al getter. Each sample was remelted several times to promote homogeneity and annealed at 800 °C for 7 days.

Table 1. Comparison of the structural data for $CeMIn_5$ and Ce_2MIn_8 series of compounds.

Atomic positions of Ce_2MIn_8 compounds				
Atom		x	y	z
Ce	2g	0	0	z_{Ce}
M	1a	0	0	0
In1	2e	0	0.5	0.5
In2	4i	0	0.5	z_{In2}
In3	2h	0.5	0.5	z_{In3}
Compound	z_{Ce}	z_{In2}	z_{In3}	
Ce_2CoIn_8 [43]	0.3105	0.1199	0.2962	
Ce_2RhIn_8 [44]	0.3070	0.1194	0.3056	
Ce_2IrIn_8 [44]	0.3060	0.1199	0.3056	
Atomic positions of $CeMIn_5$ compounds				
Atom		x	y	z
Ce	1a	0	0	0
M	1b	0	0	0.5
In1	1c	0.5	0.5	0
In2	4i	0	0.5	z_{In2}
Compound	z_{In2}			
$CeCoIn_5$ [43]	0.3103			
$CeRhIn_5$ [45]	0.3059			
$CeIrIn_5$ [45]	0.3052			

Polycrystals were examined by the x-ray powder diffraction analysis and found to consist of a single phase. Single crystals of $CeCoIn_5$ and Ce_2CoIn_8 were grown by the

self-flux method described elsewhere [42, 12], from the elemental metals (Ce 99.99%, Co 99.9%, In 99.995% in units of atomic %) using In as a flux. The quality of crystals was checked by Laue and rotating crystal methods. The lattice parameters provided in table 2 were acquired from the diffraction pattern analysis and are in agreement with those previously reported [14, 43–45].

The XPS spectra were obtained with monochromatized Al Kα radiation at room temperature using a PHI 5700 ESCA spectrometer. Total energy resolution was about 0.4 eV. Polycrystalline samples were broken under a high vacuum of 6×10^{-10} Torr immediately before taking spectra. In the case of $CeIn_3$ we also measured the sample polished in ultra-high vacuum and the sputtered one using an Ar ion beam. Calibration of the spectra was performed according to [46]. Binding energies were referenced to the Fermi level ($\epsilon_{\mathrm{F}} = 0$). A background, calculated using Tougaard algorithm [47], was subtracted from the XPS data.

4. Results and discussion

4.1. Ce 3d XPS spectra

Analysis of the Ce 3d XPS spectra is a proper method to investigate the character of the Ce 4f states in intermetallic systems owing to the strong Coulomb interaction between photoemission holes in the 3d shell and electrons located near the Fermi level. Figure 1 shows the Ce 3d XPS spectra of $CeIn_3$, $CeMIn_5$ and Ce_2MIn_8 compounds. Because of the

Table 2. Lattice parameters a and c, volume of the unit cell V, height of the $CeIn_3$ complex h_{CeIn_3}, difference between h_{CeIn_3} and a lattice parameter, and volume of the $CeIn_3$ complex for all $Ce_nM_mIn_{2m+3n}$ compounds. The table also presents values of hybridization energy Δ estimated from the Ce 3d XPS spectra.

Compound	a (Å)	c (Å)	V (Å^3)	h_{CeIn_3} (Å)	$a0h_{CeIn_3}$ (Å)	V_{CeIn_3} (Å^3)	Δ (meV)
$CeIn_3$ [14]	4.687		102.964	4.687	—	102.964	60
Ce_2CoIn_8 [43]	4.640	12.251	263.759	4.657	−0.017	100.263	89
Ce_2RhIn_8 [44]	4.667	12.247	266.750	4.661	0.006	101.521	85
Ce_2IrIn_8 [44]	4.690	12.195	268.242	4.635	0.055	101.952	—
$CeCoIn_5$ [43]	4.601	7.540	159.616	4.679	−0.078	99.051	89
$CeRhIn_5$ [45]	4.656	7.542	163.498	4.614	0.042	100.024	84
$CeIrIn_5$ [45]	4.674	7.501	163.869	4.579	0.095	100.034	89

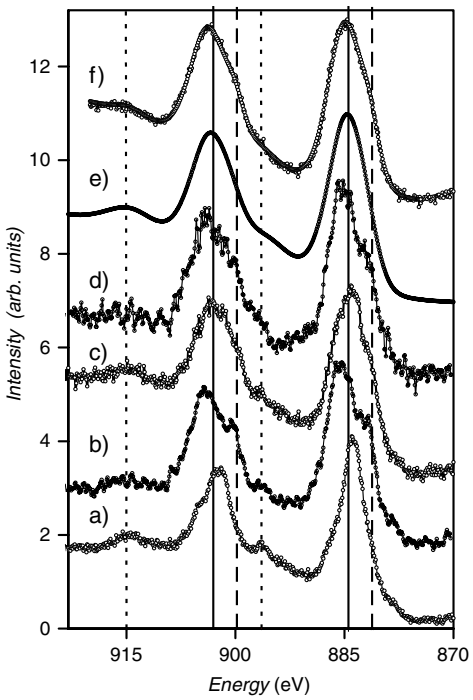

Figure 1. The Ce 3d XPS spectra for $CeIn_3$ (a), Ce_2CoIn_8 (b), Ce_2RhIn_8 (c), $CeCoIn_5$ (d), $CeRhIn_5$ (e) and $CeIrIn_5$ (f).

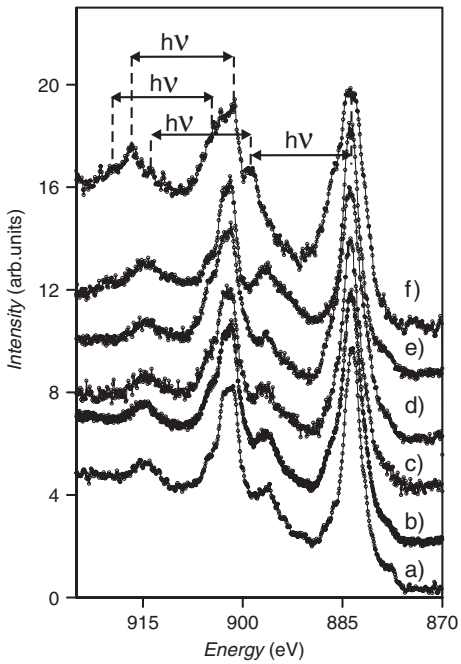

Figure 2. Ce 3d XPS spectra for $CeIn_3$ measured under low angle (a) and from the sputtered (b), polished ((c), (d)) and broken in ultra-high vacuum surfaces of the sample ((e), (f)). The satellite lines observed in the 3d XPS spectra are interpreted as plasmon losses with an energy of $h\nu \approx 13$ eV.

SO interaction there are two sets of photoemission lines in each Ce 3d XPS spectrum: $3d_{3/2}$ and $3d_{5/2}$, with intensity ratio $I(3d_{5/2})/I(3d_{3/2}) = 3/2$. The estimated value of the SO splitting (δ) is equal to 18.6 eV and is the same for all investigated compounds. Our LAPW calculations gave a similar result for the SO splitting for these compounds (δ = 18.84 eV).

Each set of photoemission lines in the Ce 3d XPS spectrum can consist of three different core-ionized final state contributions labelled as f^0, f^1 and f^2, for which the nominal f electron counts are 0, 1 or 2. The $3d^9f^1$ peaks are interpreted as the main photoemission lines. The $3d^9f^2$ components, located on the low-energy side of the main lines at a distance of ∼4 eV from the f^1 lines, originate from a screening of the core hole by electrons from the valence band to the 4f states [48–50]. Therefore the f^2 peak intensity can be considered as an indicator of hybridization strength between Ce 4f shell and conduction states. The appearance of an additional $3d^9f^0$ line in the 3d XPS spectrum, ∼11 eV away from the f^1 peaks, may be evidence of the intermediate valence behaviour of Ce [49].

In Ce 3d XPS spectra for all investigated compounds (figure 1) we found broad maxima located at the binding energies of 896.4 and 915 eV, which are 11.5–12.5 eV away from the f^1 peaks. These contributions are more pronounced in the case of $CeIn_3$. To give insight into their origin we performed consecutive XPS measurements on the $CeIn_3$ samples prepared for XPS experiments in different ways (see description of figure 2). The inelastic mean free path of the electrons with ∼600 eV kinetic energy is about 10 Å, so approximately 20% of each Ce 3d XPS spectrum measured under the angle close to 90° arises from the first atomic layer where the Ce electrons might have different electronic structure [51]. To investigate the contribution to the Ce 3d XPS spectra coming from the surface states we also performed

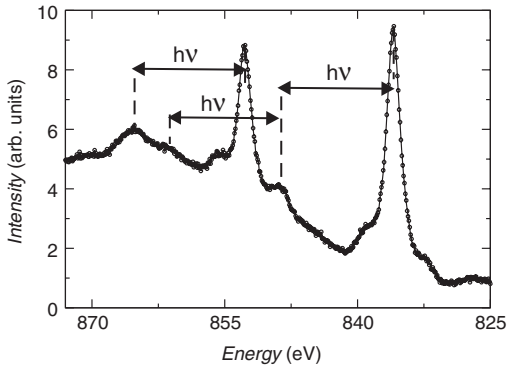

Figure 3. La 3d XPS spectra for $LaIn_3$. The additional features visible in the spectrum are interpreted as being due to the plasmon effect with an energy loss of $h\nu \approx 13$ eV.

XPS measurements under low angle on the almost flat plane of the $CeIn_3$ sample, which was broken under a high vacuum immediately before taking spectra. Results are shown in figure 2.

The intensity of the contribution located at 878 eV in the 3d XPS spectrum of $CeIn_3$ depends on the surface preparation. The features at about 905 and 887 eV we assign to the multiplet structure of the f^1 configuration due to the coupling of the 3d hole with the open 4f shell [52]. It is worthwhile to note, however, that these contributions are significantly larger in the spectrum measured under low angle. This suggests that they are pronounced in some Ce 3d XPS spectra due to the surface effects. In the Ce 3d XPS spectrum measured under low angle we also observe the appearance of additional features at about 899 and 914 eV, 917 and 920 eV. These peaks could be interpreted as plasmon loss satellites arising from group oscillations of the conduction electrons, which we indicated in figure 2.

For comparison, in figure 3 we present the La 3d XPS spectrum of the isostructural reference compound $LaIn_3$ as well. There are two main photoemission lines in the spectrum: $3d_{3/2}$ and $3d_{5/2}$, which exhibit a spin–orbit splitting δ equal to 17 eV. This value is in agreement with the one calculated by the LAPW and FPLO methods ($\delta = 17.2$ eV). The main photoemission lines in RE 3d XPS spectra are much wider for $Ce_nM_mIn_{2m+3n}$ compounds than for $LaIn_3$. The observed broadening is supposed to result from multiplet effects and a special broadening mechanism related to virtual-bound-state effects [53]. The last mechanism arises if the state from which an electron hops into a localized screening orbital from the full valence states is degenerate with the energy of a poorly screened state.

The contributions to the La 3d XPS spectrum at the binding energies of 832.5 and 849.5 eV we attribute to the screening of the core hole by the transfer of an electron from the valence band to the localized 4f states [49], while the features visible at about 893.5 and 886 eV are supposed to originate from the surface effects, like the analogous contributions in the Ce 3d XPS spectrum of $CeIn_3$. We would like to note that there are also additional peaks in the spectrum, that we interpret as the energy-loss lines (see figure 3). Some of them overlap with a very broad Auger line in the energy range of 860–870 eV.

The preceding analysis indicates the presence of plasmon effects in measured XPS Ce 3d spectra. Since the shape of the peaks located at about 896.4 and 915 eV and the interval in energy between them and the f^1 lines are very similar to those of the peaks interpreted as energy-loss lines [49], we assign them to plasmon satellites of the main photoemission lines. We did not find any additional, sharp peaks in the measured Ce 3d spectra in a similar energy range which could be interpreted as f^0-like peaks, providing clear evidence of a mixed valence of Ce in the investigated compounds. It is worthwhile to stress that for $CeRhIn_5$ and $CeIrIn_5$ compounds this judgement is consistent with XAS results [19]. In case of the parent $CeIn_3$ compound the stable valence of Ce is also in agreement with previous experimental results (e.g. NQR, 2D angular correlation of the electron–positron annihilation radiation), which unambiguously revealed that Ce 4f states in $CeIn_3$ are well localized at ambient pressure [28–30]. Moreover, significant deviations from Vegard's law in $CeIn_{3-x}Sn_x$ have been attributed to the valence transition from trivalence for $x < 2.3$ to a small amount of mixed valence character for $x > 2.3$, also pointing to the stable Ce^{+3} configuration in $CeIn_3$ [54]. However, we cannot exclude a very slight mixed valence effect in all investigated compounds, because in the Ce 3d core-level XPS spectra the loss-energy lines and peaks connected to the $3d^94f^0$ configuration of Ce could overlap.

Gunnarsson and Schönhammer (GS) [55, 49] have shown how the experimental Ce 3d spectra can be used to estimate the hybridization energy Δ between the 4f and conduction electron states. The hybridization energy Δ is defined as $\pi V^2 \rho_{\max}$, where $\rho_{\max}$ is the maximum value of the DOS and V is the hybridization matrix element in the Anderson impurity Hamiltonian. According to the GS theory, the ratio $R = I(f^2)/(I(f^1) + I(f^2))$, where $I(f^n)$ is the intensity of the f^n peak, provides a sensitive measure of Δ. The dependence of R on the shape of the conduction band and the n_f value as well as the other model parameters is much weaker than on the Δ value [55]. Therefore, based on figures 5 and 6 of [49], we have estimated the values of the energy Δ for $Ce_nM_mIn_{2m+3n}$ compounds, assuming their conduction band's DOS to be a simple semi-elliptic one with lower edge $B^- = 4$ eV and upper edge $B^+ = 1.57$ eV with respect to the Fermi level. The other parameters in the GS model were assumed to take values typical for Ce-based intermetallics (the Coulomb interaction between the core hole and the 4f subshell $U_{fc} \cong 9.6$–13.0 eV and $U = 6.4$ eV). The separation of the overlapping peaks in Ce 3d XPS spectra was done on the basis of the Doniach–Šunjić theory using the same parameters for all systems [56]. The energy distance between f^1 and f^2 peaks was found to be ~3.5 eV. The obtained Δ values are listed in table 2.

The estimated values of the hybridization energy Δ should not be treated dogmatically, since they are only as good as the GS theoretical model used to extract them. Moreover, there are many other sources of errors in estimation of Δ values. The most important ones we attribute to the surface contribution to the measured spectra, the spectrum decomposition and the background subtraction. Besides, in order to estimate the Δ

values we assumed simple semi-elliptical conduction bands of the investigated compounds. Substitution of the true densities of states could change the deduced Δ values even by up to 20–30% [49, 55].

Finally, we are aware of the fact that the absolute values of the hybridization energy Δ, listed in table 2, can differ by a factor of up to two from those found in other experiments [55]. It is worth noting, however, that based on the 3d–4f and 4d–4f RPES experiments and using the non-crossing approximation of the Anderson impurity model Kim *et al* [57] found the Δ value for bulk $CeIn_3$ to be about 69 meV and about 47 meV for surface states. Our estimations (table 2) gave the hybridization energy as slightly reduced as compared to the bulk value of Kim *et al*, which may be mainly due to the surface contributions to the XPS spectra. Furthermore, the Δ values listed in table 2 were obtained using the same procedure, i.e., the samples were prepared in a similar way, measured under similar conditions, the Ce 3d XPS spectra were analysed and deconvoluted in an analogous way. Therefore it is justified to compare the estimated Δ values in order to analyse the changes in hybridization strength, related to the changes in the f^2 peak weight in Ce 3d XPS spectra of the investigated compounds.

Hybridization energy Δ is similar for $CeMIn_5$ and Ce_2MIn_8 compounds and much bigger than for the parent $CeIn_3$. This is consistent with previous conclusions suggesting that in $CeIn_3$ the character of Ce 4f states is well localized [28–30], while in $CeMIn_5$ compounds these states are on the border of localization [19]. Our results suggest that there are also slight variations in hybridization strength within $CeMIn_5$ and Ce_2MIn_8 compounds. In both subfamilies, the estimated hybridization energy is a bit smaller for compounds containing Rh than for their counterparts with Co and Ir. Since the observed changes in hybridization strength within $CeMIn_5$ and Ce_2MIn_8 subfamilies are very similar and these changes have been also confirmed by the other comparative spectroscopic studies [19, 58], we believe that they are meaningful. It is of great interest to understand the mechanisms leading to the observed changes in hybridization energy Δ within the $Ce_nM_mIn_{2m+3n}$ compounds.

For $Ce_nM_mIn_{2m+3n}$ systems, one of the most important factors having an influence on Δ value and ground state properties could be the volume of the $CeIn_3$ complex. For the parent $CeIn_3$ compound, for instance, the contraction of unit cell volume (due to application of external pressure) leads to transition from the AF ground state to the non-magnetic ones, which is connected with the Δ enhancement and the delocalization of Ce 4f states [5].

Much stronger hybridization Δ for all $CeMIn_5$ and Ce_2MIn_8 compounds in relation to that for the parent $CeIn_3$ (table 2) could also be partially explained as due to the so called *chemical pressure effect*, i.e. the changes of $CeIn_3$-complex volume induced by the inserted MIn_2 layers. However, the variation in volume of the $CeIn_3$ complex between $CeIn_3$ and Ce_2MIn_8 compounds is comparable with that between $CeMIn_5$ and Ce_2MIn_8 series (table 2), but no significant difference in the hybridization energy Δ between the last two subfamilies can be observed. This suggests that the variation in the $CeIn_3$-complex volume is not the only mechanism responsible for the observed variation in the hybridization energy across the investigated compounds.

Moreover, the slight strengthening of the hybridization Δ for $CeCoIn_5$ and $CeIrIn_5$ with respect to $CeRhIn_5$, suggested by the Ce 3d XPS spectra, is in agreement with the fact that systems with Co and Ir at ambient pressure exhibit similar properties (HF SC) [10, 11] as $CeRhIn_5$ under external pressure [6–9]. However, only the enhancement of Δ for $CeCoIn_5$ with respect to $CeRhIn_5$ could be attributed to the *chemical pressure effect*. Meanwhile, $CeIrIn_5$ and $CeRhIn_5$ have similar volumes of the $CeIn_3$ complexes (see table 2), despite the difference in hybridization strength Δ. Therefore, we conclude that the *chemical pressure effect* cannot be the single mechanism responsible for the strength of hybridization between 4f states and the conduction band in the investigated family of compounds.

The slight enhancement of hybridization energy Δ for $CeIrIn_5$ and $CeCoIn_5$ with respect to that for $CeRhIn_5$ could be connected with the tetragonal distortion of the $CeIn_3$ cuboctahedra. According to the distortion parameter (a-h_{CeIn_3}), shown in table 2, the $CeIn_3$ complexes in all $CeMIn_5$ compounds are distorted with respect to the parent $CeIn_3$ composition. However, for $CeCoIn_5$ and $CeIrIn_5$ compounds the distortion is much larger than for $CeRhIn_5$. This might indicate that in these compounds the increase in distortion of the $CeIn_3$ cuboctahedra favours the strengthening of the hybridization parameter Δ and the formation of the SC ground state. On the other hand, smaller distortion (as in $CeRhIn_5$) or higher Ce point symmetry (as in $CeIn_3$) favours the AF ground state, as suggested previously [45]. Similar tendency can be also observed in Ce_2MIn_8 subfamily (table 2).

Nevertheless, taking into consideration both the *chemical pressure effect* and the distortion of $CeIn_3$ cuboctahedra, we still cannot explain why for instance Ce_2CoIn_8 is an HF SC with a relatively strong hybridization Δ, while $CeRhIn_5$ shows the AF ground state and slightly smaller Δ value. Since the volume of $CeIn_3$ complexes is smaller in $CeRhIn_5$ than in Ce_2CoIn_8 and distortion of the $CeIn_3$ cuboctahedra is not significant for both compounds (smaller for Ce_2CoIn_8), one would expect an SC ground state and stronger hybridization Δ for $CeRhIn_5$ rather than for Ce_2CoIn_8, which do not agree with experimental data.

Therefore, we guess that inclusion of transition metal atoms, besides leading to both shape distortion and volume contraction of the $CeIn_3$ cuboctahedra, must have also a direct influence on the Ce 4f states due to the formation of bondings between Ce and the nearest neighbouring (NN) M atoms. This conclusion has been supported by the band character analysis as well as the *valence charge density* analysis, presented in sections 4.3 and 4.4. An important question, which should be answered, concerns the overall mechanism responsible for changes in ground state properties within the whole family of compounds and leading, on the one hand, to the significant rise in hybridization between the Ce 4f states and conduction band in $CeMIn_5$ and Ce_2MIn_8 subfamilies as compared to that in parent $CeIn_3$ compound and, on the other hand, to the slight variation of the hybridization strength within both $CeMIn_5$ and Ce_2MIn_8 subfamilies. Our band structure results and *valence*

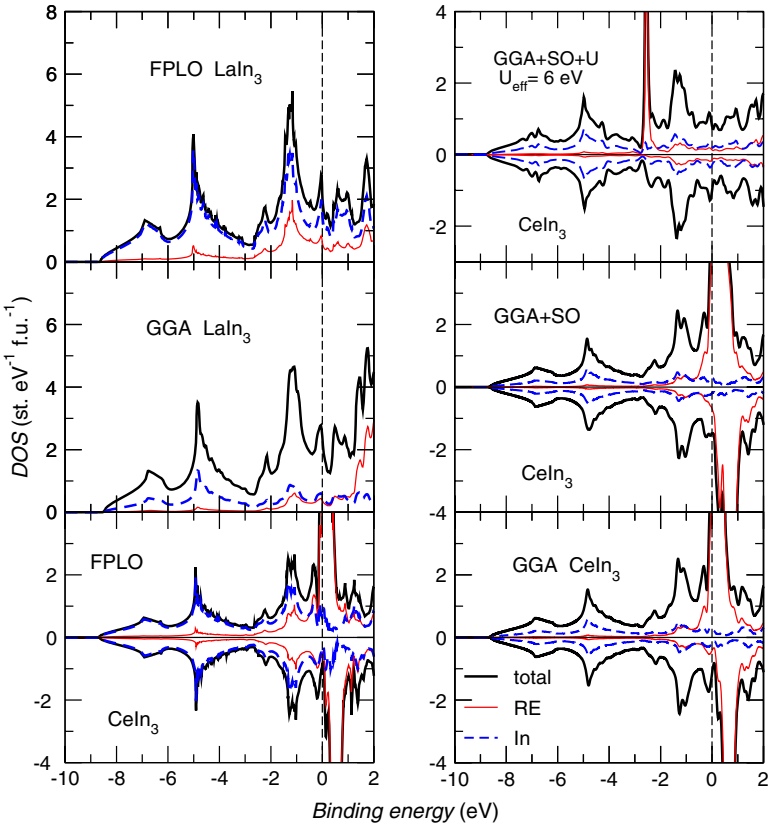

Figure 4. The calculated (LAPW and FPLO) total and atom projected density of states of $CeIn_3$ and $LaIn_3$. For $CeIn_3$ the majority (minority) spin was plotted upward (downward). The common vertical dashed line indicates the position of the Fermi level (colour online).

Table 3. $CeIn_3$: density of states at ϵ_F–DOS(ϵ_F); Ce 4f contribution to the DOS at ϵ_F − DOS_{4f} (ϵ_F); Sommerfeld coefficient γ calculated from the DOS(ϵ_F); the spin (M_S), orbital (M_L) and total (M_J) magnetic moments of Ce obtained by the LAPW method within different approximations, assuming the ferromagnetic (FM) or antiferromagnetic (AFM) order.

	FM	+SO	+SO + U $U_{eff} = 6$ eV	AFM	+U $U_{eff} = 6$ eV
DOS(ϵ_F) (states eV^{-1} f.u.$^{-1}$)	8.3	10.7	2.1	9.8	2.3
DOS_{4f} (ϵ_F) (states eV^{-1} f.u.$^{-1}$)	6.4	8.2	0.04	9.3	0.06
γ (mJ mol^{-1} K^{-2})	19.6	25.3	4.8	23.2	5.4
M_S (μ_B)	0.64	0.60	0.99	0.69	0.99
M_L (μ_B)	—	−0.50	−0.52	—	—
M_J (μ_B)	—	0.10	0.47	—	—

charge density distribution, discussed in the next sections, give insight into this problem.

4.2. Valence band of $CeIn_3$

Figure 4 shows the total and partial electronic densities of states (DOSs) for $CeIn_3$ calculated by the LAPW method, assuming the ferromagnetic (FM) spin polarization. The SO interaction results only in a slight reduction of the Ce spin moment (table 3) due to the SO splitting of the Ce 4f bands. The characteristic feature of the DOSs obtained within the GGA and GGA + SO approximations is the unrealistic narrow bands near the Fermi level formed mainly by the Ce 4f states due to the insufficient treatment of the Coulomb correlations within the 4f manifold by the GGA approach. In contrast, the Ce 3d XPS spectra has revealed that the Ce atoms have a trivalent configuration in $CeIn_3$, suggesting the strongly correlated character of the 4f states. Therefore we applied the GGA + SO + U approach to the Ce 4f states to account for the strong correlations within this shell. The Hubbard-type correlation term included in the XC potential splits the occupied and unoccupied 4f bands and shifts them away from the Fermi level. Consequently, it modifies essentially the hybridization between the Ce 4f and valence band states close to the Fermi level, reduces the DOS at the Fermi level and leads to the increase of the Ce spin moment (table 3).

The calculations with the Hubbard parameter values U_{eff} larger than about 4 eV yield the qualitatively correct description of the trivalent Ce in $CeIn_3$, with approximately one electron occupying the 4f shell and the magnetic spin moment of Ce equal to ~ 1 μ_B. For $U_{eff} \approx 6$ eV, which is typical for Ce^{3+} [59], the occupied 4f states form a narrow peak

at about 2.7 eV below ϵ_F (figure 4), but there is still some slight contribution of these states near the ϵ_F due to the hybridization with the conduction band. In the band structure (figure 9) there is a small, uniform admixture of the Ce 4f band character for several bands close to the Fermi level. Near the R point in the Brillouin zone there is also a distinct hybridization between the main occupied Ce 4f and some In 4p states, located in the same energy region. This might indicate that the 4f electrons contribute to the bonding in $CeIn_3$.

The variation of the U_{eff} parameter within the range of 4–8 eV, besides the shift of the main 4f band on the energy scale and slight changes of the hybridization around the R point, almost does not affect the overall shape of the band structure, which justifies the GGA + SO + U description.

It is worthwhile to note that the experimental value of the Sommerfeld coefficient of 130 mJ (mol K^2)$^{-1}$ for $CeIn_3$ [60] is an order of magnitude larger than the theoretical one obtained from the DOS(ϵ_F) (table 3). Different effects, e.g. phonon–electron coupling or magnetic excitations, can enlarge the γ-value, but such a strong enhancement of the Sommerfeld coefficient suggests that at low temperatures there is a peak of the electronic quasi-particle density of states at the Fermi level originating from the Abrikosov–Suhl resonance. This effect cannot be described within the GGA + U approach, which is a mean-field-like approximation and neglects all the dynamic correlation effects.

The calculated spin moment of In is negligible, manifesting that only Ce atoms carry magnetic moment in $CeIn_3$, in agreement with the experimental data [14]. The theoretical values of spin, orbital and total magnetic moments of Ce are listed in table 3. Since at low temperatures $CeIn_3$ orders antiferromagnetically, we also performed AF band structure calculations. According to the experimental data [14] we assumed the simple AF structure of type II, where Ce magnetic moments align antiferromagnetically in adjacent (111) FM planes. The AF coupling between Ce moments leads to the slight increase of the DOS(ϵ_F) and of the spin moment of Ce within both the GGA approximation and the GGA + U approach applied for the Ce 4f states (see table 3). The FM and the AF solutions have similar total energies, that correlate with the low value of $T_N = 10.2$ K for $CeIn_3$. We got a quantitative agreement between the calculated and experimental [14] total magnetic moments of Ce only within the GGA + U approach with the value of the U_{eff} parameter typical for the rare earth elements. This suggests the strongly correlated character of Ce 4f states in $CeIn_3$. This result has been confirmed by the XPS valence band spectrum (figure 5).

To analyse in detail the experimental data we have calculated the XPS spectra based on the theoretical partial DOS data obtained by the LAPW method in both the GGA approximation and using the GGA + U approach for the Ce 4f states. Results are shown in figure 5(c). The peaks located at about 4.9 and 6.8 eV are attributed mainly to the In 5s states, while the main feature, with a maximum at about 1.5 eV, originates from the In 5p bands hybridized with the Ce 5d and Ce 4f states. The width of the features in the measured photoemission spectrum is larger than that expected theoretically. This could indicate that the experimental

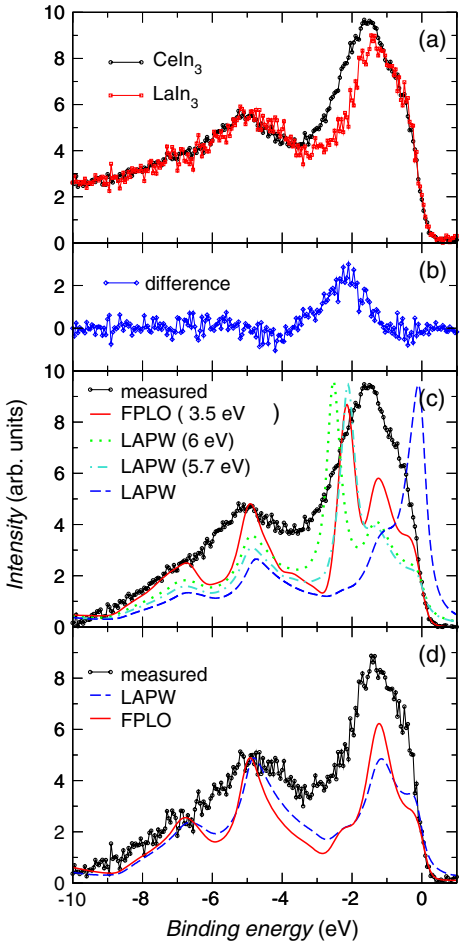

Figure 5. The XPS valence band spectra of $CeIn_3$ and $LaIn_3$ (a) and the difference between these two spectra (b). In panels (c) and (d), respectively, the XPS valence band spectra of $CeIn_3$ and $LaIn_3$, corrected by the background, are compared with the calculated ones based on the FPLO and LAPW DOSs. For $CeIn_3$ different values of the U_{eff} parameter were assumed for Ce 4f states (colour online).

resolution was slightly worse than assumed in calculations. Furthermore, a significant discrepancy between the theoretical and measured XPS valence bands can be observed with regard to the intensities of features located near the Fermi level. To understand the reason for this disagreement we performed the XPS experiments on the isostructural reference $LaIn_3$ compound and additional band structure calculations by the FPLO method for both $CeIn_3$ and $LaIn_3$. In figure 5(a) we present a comparison between the XPS valence band spectra measured for $LaIn_3$ and $CeIn_3$. The experimental data were normalized to the common intensity of peak located at about 4.9 eV originating from In states. The difference between the two spectra occurs only in the binding energy range from −4 to −1 eV. Since band structure calculations revealed similar shapes of the DOSs for $CeIn_3$ and $LaIn_3$ except the 4f contribution of the rare earth (RE) elements (figure 5), we have attributed the difference between the two spectra (shown in figure 5(b)) mainly to the Ce 4f states. According to the XPS data, the Ce 4f states form a wide peak located at the binding energy of 2.1 eV. This value is slightly higher than that previously reported on the basis

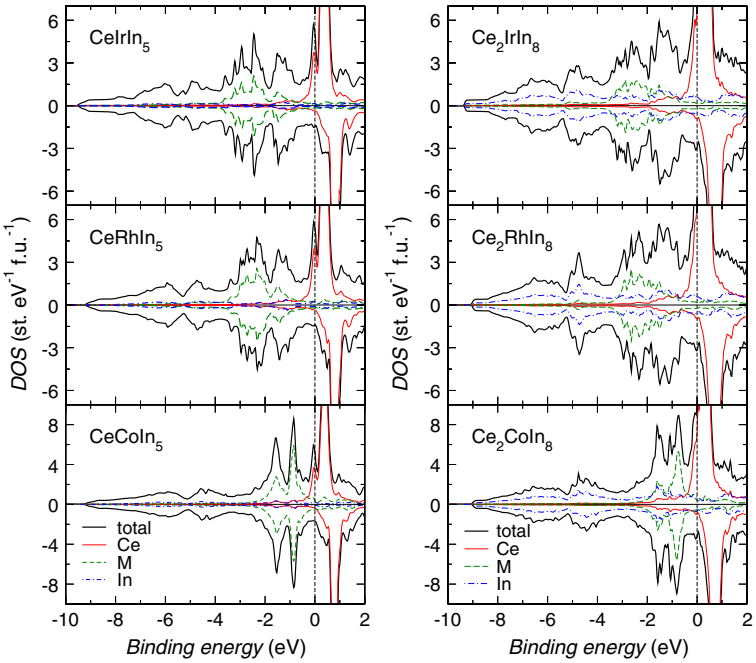

Figure 6. The total and atomic, spin projected density of states of $CeMIn_5$ and Ce_2MIn_8 compounds calculated by the LAPW method within the GGA approximation. Detailed description as in figure 4 (colour online).

of the 4d–4f RPES experiments and the many-body model calculations (∼1.5 eV) [57]. Our band structure calculations reproduced the experimental energy position of the occupied Ce 4f states when the Coulomb correlation parameter U_{eff} for this states takes the value of 4.7 and 3.5 eV within the LAPW and the FPLO method, respectively (figure 5(c)). This confirms the strongly correlated character of the 4f bands in $CeIn_3$. The difference between the $CeIn_3$ and $LaIn_3$ valence band spectra (figure 5(b)), however, is much wider than the calculated Ce 4f contribution to the valence band spectrum. The observed discrepancy could result for instance from disorder in the polycrystalline sample, grain boundary effects or the surface contribution to the measured spectra.

Let us consider the discrepancy between the theoretical XPS valence band spectra obtained by the LAPW and the FPLO method (figures 5(c) and (d)). Concerning the total DOS of $CeIn_3$ and $LaIn_3$ both methods gave very similar results (figure 4). The differences between the LAPW and FPLO based spectra originate mainly from the interstitial region in the LAPW method, that cannot be taken straightforwardly into account in calculations of the theoretical XPS spectra based on the partial atom-*l*-resolved DOSs. The FPLO crystal potential does not introduce the interstitial regions. Therefore, for both investigated compounds the FPLO method gave better agreement between the theory and experiment at the low binding energies. The compatibility between the calculated and measured XPS valence bands, however, is still not satisfactory with regard to the peak intensities. The discrepancies are similar for $CeIn_3$ and $LaIn_3$. This could suggest that in the case of these compounds the photoemission cross-sections differ strongly

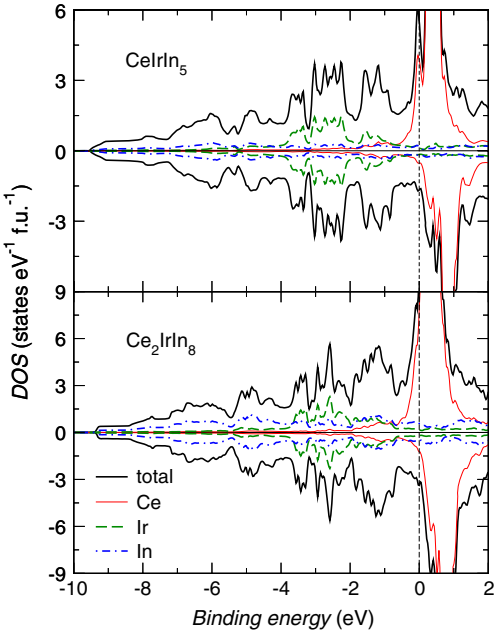

Figure 7. The total and atomic, spin projected density of states of Ce_2IrIn_8 and $CeIrIn_5$ compounds calculated by the LAPW method within the GGA approximation including the spin–orbit coupling. Detailed description as in figure 4 (colour online).

from that of Yeh and Lindau obtained from the atomic-like calculations [41].

4.3. Valence band of $CeMIn_5$ and Ce_2MIn_8

Results of *ab initio* calculations for both subfamilies are summarized by figures 6–10 and listed in tables 4 and 5.

Table 4. Density of states at ϵ_F-DOS(ϵ_F), calculated (γ) and experimental (γ_{exp}) values of Sommerfeld coefficient, spin magnetic moment (M_S) of Ce obtained by the LAPW method within the GGA approximation and using the GGA + SO + U ($U_{eff} = 6$ eV) approach for $CeMIn_5$ and Ce_2MIn_8 compounds.

	DOS(ϵ_F) (states eV^{-1} f.u.$^{-1}$)		γ (mJ mol^{-1} K^{-2})			M_S [Ce] (μ_B)	
Compound	GGA	+SO + U	GGA	+SO + U	γ_{exp}	GGA	+SO + U
$CeCoIn_5$	7.0	2.4	16.5	5.7	≈1200 [10]	0.71	0.99
$CeRhIn_5$	6.8	2.1	16.0	4.9	≈400 [7]	0.74	0.99
$CeIrIn_5$	6.6	2.1	15.5	4.9	≈720 [7]	0.73	0.99
Ce_2CoIn_8	13.1	5.1	30.9	12.0	>500 [12]	0.66	0.99
Ce_2RhIn_8	13.6	4.5	32.0	10.6	≈ 400 [7]	0.68	0.98
Ce_2IrIn_8	12.8	5.0	30.1	11.8	≈ 700 [65, 7]	0.68	0.99

Table 5. $CeRhIn_5$ and Ce_2RhIn_8: density of states at ϵ_F-DOS(ϵ_F); the spin (M_S), orbital (M_L) and total (M_J) magnetic moments of Ce obtained by the LAPW method within the GGA approximation and taking into account the spin–orbit coupling (+SO) and the strong correlation interaction within Ce 4f states (+U), assuming the ferromagnetic (FM) or antiferromagnetic (AF) order.

$CeRhIn_5$	FM	+SO	+SO + U	+SO + U	+SO + U	+SO + U	AF	+U
U_{eff} (eV)	—	—	0.35	1	2.85	6	—	6
DOS(ϵ_F) (states eV^{-1} f.u.$^{-1}$)	6.8	7.1	6.5	3.7	2.3	2.1	9.2	2.13
M_S (μ_B)	0.74	0.70	0.84	0.89	0.95	0.99	0.71	0.99
M_L (μ_B)	—	−0.47	−0.64	−0.51	−0.49	−0.51	—	—
M_J (μ_B)	—	0.23	0.20	0.38	0.46	0.48	—	—
$CeRhIn_5$	FM	+SO	+SO + U	+SO + U	+SO + U	+SO + U	AF	+U
U_{eff} (eV)	—	—	0.85	1.4	2.35	6	—	6
DOS(ϵ_F) (states eV^{-1} f.u.$^{-1}$)	13.6	14.4	6.5	5.4	4.9	4.5	14.6	4.6
M_S (μ_B)	0.68	0.64	0.89	0.93	0.95	0.98	0.72	1.00
M_L (μ_B)	—	−0.44	−0.51	−0.46	−0.47	−0.50	—	—
M_J (μ_B)	—	0.20	0.38	0.47	0.48	0.48	—	—

Figure 6 presents the total and partial electronic density of states (DOS) of $CeMIn_5$ and Ce_2MIn_8 (M = Co, Rh or Ir) compounds calculated within the GGA approximation. The spin-polarized band structure calculations reveal a magnetic ground state with significant magnetic moments only on Ce atoms for all investigated compounds (table 4).

Inclusion of the SO interaction causes a reduction of the Ce spin moment and a small increase of the DOS(ϵ_F) due to the splitting of the Ce 4f bands. It has no significant influence on the shape of the other partial DOSs, except the 5d states of Ir in $CeIrIn_5$ and Ce_2IrIn_8 (see figure 7). The SO coupling splits a complex of these bands, located at energies of 2–4 eV, into two separate parts and results in a shift of these states to higher binding energy. The experimental XPS valence band spectrum for $CeIrIn_5$ has confirmed this effect (see figure 10 and discussion below).

For all $CeMIn_5$ and Ce_2IrIn_8 systems the partial Ce 4f DOSs obtained within the GGA approximation are pinned in the vicinity of the Fermi level and give significant contributions to the DOS(ϵ_F). This outcome is inconsistent with the XPS results (section 4.1), which pointed to the Ce in a trivalent state for all investigated compounds. Application of the GGA + SO+U method circumvents this problem by including the Hubbard-like interaction term in the XC potential for the Ce 4f shell. It results in a shift of the occupied Ce 4f bands toward higher binding energies and of the unoccupied 4f states above the Fermi level and for a reasonable range of the U_{eff}-values (4–8 eV) it provides the correct physical picture of trivalent Ce state with one electron occupying the 4f orbital for all $CeMIn_5$ and Ce_2MIn_8 compounds. For this range of U_{eff}-values the shape of the partial DOSs for all atoms except Ce almost does not depend on this parameter, especially in a region close to the Fermi level, which is crucial for the low-energy excitations. The calculated spin moments of M and In atoms are smaller than 0.05 μ_B for all examined compounds. The obtained values of Ce magnetic moments are listed in tables 4 and 5. The calculated DOS(ϵ_F) are very similar within both series of $CeMIn_5$ and Ce_2MIn_8 compounds (table 4).

For $U_{eff} \sim 6$ eV (typical for Ce^{3+}) the occupied 4f states form a narrow band at about 2.7 eV for all $CeMIn_5$ and Ce_2MIn_8 systems (figure 8). There is still, however, some slight contribution of these states near ϵ_F due to the hybridization with the conduction band. The traces of such hybridization can be seen in figure 9. Detailed analysis of partial weights of the band states for $CeRhIn_5$ (figures 9(b) and (c)) shows that the band located just below −0.4 eV near Γ is of mixed character. Although the dominant contribution at Γ comes from the In2 p states, the admixture of the Ce 4f character is also significant. This hybridized complex changes its orbital character gradually to Rh 4d as one goes away from Γ. Application of the larger U_{eff}-values leads to the decrease of the admixture of the Ce 4f character in this band. Similar results were obtained for other $CeMIn_5$ compounds. For the Ce_2MIn_8 series we found pronounced admixture of Ce 4f

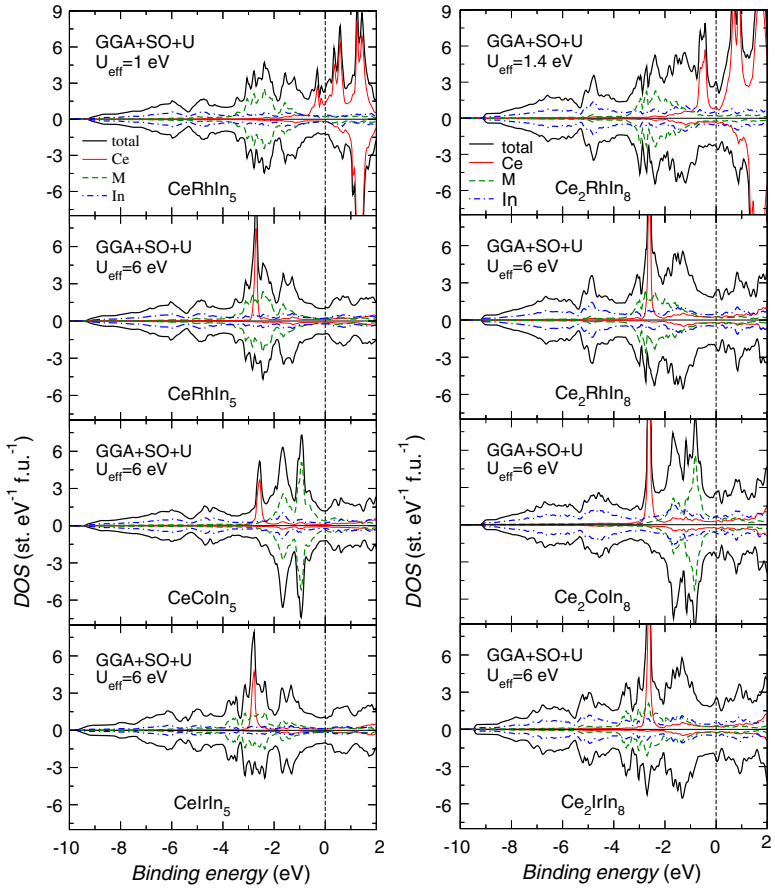

Figure 8. The total and atomic, spin projected density of states calculated by the LAPW method within the GGA + SO + U approach for $CeMIn_5$ and Ce_2MIn_8. Detailed description as in figure 4 (colour online).

character in the band at about −0.6 eV near the Z point of the Brillouin zone, in which the dominant contribution comes from the In1 p and In2 p states. This hybridized complex transforms its orbital character to M d as one goes away from Z. Figure 9(d) shows this effect in Ce_2CoIn_8. All these findings indicate that there is a hybridization between Ce f and M d states for all $CeMIn_5$ and Ce_2MIn_8 systems. This hybridization could be relevant for the changes in hybridization energy Δ within the family of investigated compounds, indicated by the XPS measurements (section 4.1).

At low temperatures $CeRhIn_5$ and Ce_2RhIn_8 are magnetically ordered. Below $T_N \approx 3.8$ K magnetic moments of Ce ions in $CeRhIn_5$ with magnitude $\sim 0.37\mu_B$ form an incommensurate transverse spiral with wavevector (1/2, 1/2, 0.297) [61], while the magnetic structure of Ce_2RhIn_8 below $T_N \sim 2.8$ K is closely related to that of cubic $CeIn_3$. In Ce_2RhIn_8 magnetic moments of Ce $\sim 0.55\ \mu_B$ are pointed 52° from the a–b plane [62]. The neutron diffraction experiments performed by Bao *et al* [63] also revealed the presence of additional peaks associated with incommensurate magnetic ordering in a very low temperature region (below ∼1.4 K). In both compounds the strongest magnetic interactions are within $CeIn_3$ layers and result in the AF ordering of the Ce magnetic moments in basal planes. The $CeIn_3$ layers are coupled weakly by an interlayer exchange interaction through the $RhIn_2$ layer. To get insight into the magnetic properties we performed band structure calculations for $CeRhIn_5$ and Ce_2RhIn_8 assuming simple AF order inside the a–b planes and along the c axis. Band structure calculations revealed that the AF interactions between Ce atoms are the reason for small changes of the Ce spin moments calculated within both GGA and GGA + U ($U_{eff} = 6$ eV) approximations (see table 5). For both compounds the FM and AFM solutions have similar total energies, that are consistent with the low values of the T_N for both compounds.

The best agreement between the calculated and experimental total magnetic moment of cerium in $CeRhIn_5$ was achieved for $U_{eff} \sim 1$ eV, which corresponds to the nearly localized nature of the Ce f electrons (figure 8). However, for the larger U_{eff}-values the theoretical Ce magnetic moment is only slightly larger (by ∼0.1 μ_B) than that estimated from the experimental results [61]. Meanwhile, for Ce_2RhIn_8, the agreement between the theoretical and experimental magnetic moments of cerium in this compound was obtained assuming the value of the U_{eff} parameter to be larger than 1.4 eV.

We compared the numerical valence band spectra obtained from our calculations with the XPS spectra. The theoretical XPS valence bands were calculated according to the description presented in section 2. The main peaks in XPS spectra, at about 2.5 eV for $CeRhIn_5$ and Ce_2RhIn_8, 2.8 eV for $CeIrIn_5$ and 1.2 eV for Ce_2CoIn_8, originate to a large extent from the d states of transition metal atoms hybridized with some of the In 5p states. The other peaks located at binding

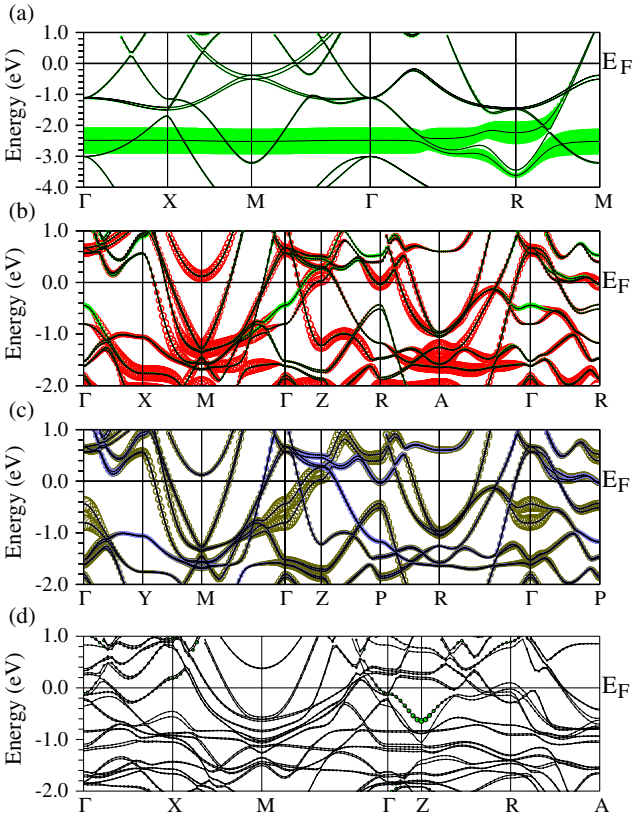

Figure 9. Electronic band structure close to the Fermi level for $CeIn_3$ (a), $CeRhIn_5$ ((b), (c)) and Ce_2CoIn_8 (d) calculated within the GGA + SO + U approach with U_{eff} =6 eV. The size of the circles denotes the weights of contributions of states with different atomic and orbital characters. In the following panels the circles represent the following: ((a), (b), (d)) green (grey) filled circles—Ce 4f; (b) red (light grey) empty circles—M d; (c) blue (dark grey) filled circles—In1 p; (d) brown (light grey) empty circles—In2 p. The radii of the circles are normalized to the radius of circles representing the Ce 4f contribution in $CeIn_3$ shown in panel (a). The high symmetry points are labelled according to the standard notation (colour online).

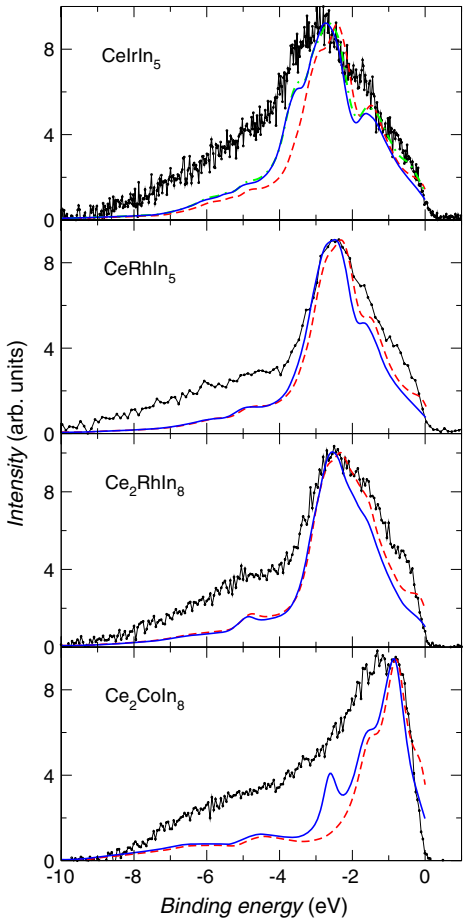

Figure 10. Comparison of the experimental XPS valence band spectra (line with points) with the theoretical ones calculated within the GGA approximation (dashed line) and using the GGA + U approach for $U_{eff} \approx 6$ eV (solid line) for Ce_2CoIn_8, Ce_2RhIn_8, $CeRhIn_5$ and $CeIrIn_5$. For $CeIrIn_5$ we also present the theoretical XPS spectrum calculated within the GGA + SO approximation (dash–dot line) (colour online).

energies 4.5–4.9 eV and 6.0–6.3 eV come mainly from the In 5s bands. The Ce 5d bands contribute in the binding energy range from about 2 eV to ϵ_F. The Ce 4f electrons give only a small contribution to the valence band spectrum, in comparison with d states of transition metals. This makes it difficult to get precise information about the Ce 4f states in $CeMIn_5$ compounds from the XPS valence band spectra. We have found a good agreement between the theoretical and experimental valence bands. The slight discrepancy visible for compounds with Rh and Ir at low binding energies up to 2 eV below the Fermi level is similar to that observed for $CeIn_3$ and $LaIn_3$ at the same binding energies (see the discussion in section 4.2). It is also worthwhile to note that taking into account the spin–orbit splitting we could reproduce the experimentally observed shape of the main peak in the XPS valence band of $CeIrIn_5$, which originates from Ir 5d states (figure 7). This confirms the important influence of this interaction on the Ir 5d bands.

Finally, the most significant difference in calculated DOSs for different compounds within the $CeMIn_5$ and Ce_2MIn_8 subfamilies is related to the d states of transition metal atoms (see figure 6). For $CeCoIn_5$ and Ce_2CoIn_8 the 3d states, located not far from the Fermi level, form narrow bands of width approximately 2 eV. In systems with Rh and Ir the d states of the M atoms reach higher binding energies and are much wider. In the case of $CeIrIn_5$ and Ce_2IrIn_8 the 3d-type bands are slightly wider than in $CeRhIn_5$ and Ce_2RhIn_8. These changes in shape of the M d bands have been confirmed by the XPS valence band measurements (see figure 7). One could explain them as follows. Transition metal atoms form layers which are parallel to the basal plane of the unit cell. Substitution of Co by larger, isoelectronic Rh results in an increase of the spatial overlapping of the d states of the neighbouring transition metal atoms. In consequence it leads to an increase in the band width and could result in changes of the hybridization of these bands with some In p states, which are located in the same region of binding energies. The difference in shape of the d bands between Rh and Ir is much smaller than that between Co and Rh for both $CeMIn_5$ and Ce_2MIn_8 subfamilies, which corresponds well to the differences in covalent radii of the M atoms (∼126 pm for Co, ∼135 pm for Rh and ∼137 pm for Ir).

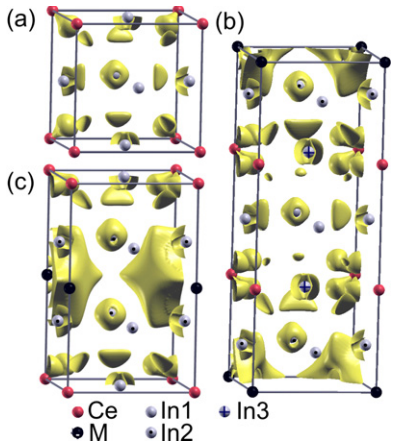

Figure 11. The surface of constant difference charge density equal to 0.0022 (electron au^{-3}) for $CeIn_3$ (a), Ce_2CoIn_8 (b) and $CeRhIn_5$ (c) calculated by the LAPW method within the GGA + SO + U ($U_{\rm eff}$ = 6 eV) approximation. Because of symmetry, only half of the unit cell is considered (colour online).

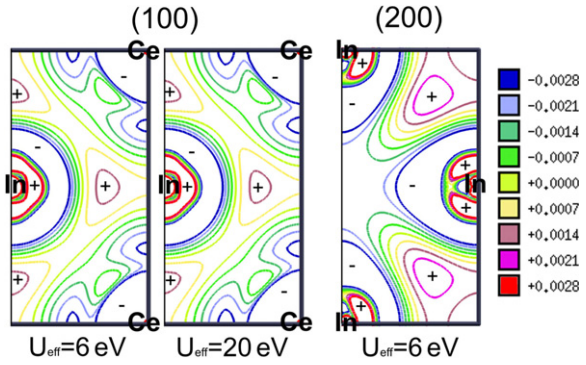

Figure 12. The difference charge densities (electron au^{-3}) for planes (100) and (200) of $CeIn_3$ calculated by the LAPW method within the GGA + SO + U approximation. Because of the symmetry properties, only part of each picture is presented. The black thick lines indicate the border of the unit cell. By + and − we denote the positive and negative values of the difference charge density. Since there is no noticeable difference between the maps for (200) planes for $U_{\rm eff}$ equal to 6 and 20 eV, we present only one of these maps (colour online).

To investigate in detail the observed changes in valence band states we performed a study of the *valence charge density* distribution for all $Ce_nM_mIn_{2m+3n}$ compounds.

4.4. Charge densities

Charge density analysis is an appropriate tool for getting insight into the bonding nature of solids. In order to study the charge distribution in all $Ce_nM_mIn_{2m+3n}$ systems we have calculated the spatial *valence charge densities* for the investigated compounds using WIEN2k computer code [33]. We have further calculated the *difference charge density* plots by subtracting the superposition of free atom densities from the self-consistent *valence charge density*. The results are shown in figures 11–14.

The *difference charge densities* illustrate the reordering of electronic density accompanying the bonding formation in the solid. Moreover, besides indicating the charge transfer, they emphasize the slight differences in charge density, especially in interatomic regions, which cannot be easily visualized using *valence charge density* maps. Therefore we base the further analysis on the *difference charge density plots*. This approach is fully justified in a quantitative analysis of the changes in charge densities calculated for a given compound using different computational set-up. The comparative analysis of *difference charge density* maps calculated for different systems is possible only on a qualitative level.

To inspect the contribution of the Ce 4f electrons to bonding we have calculated also *charge density* maps based on the band structure calculations within the GGA + SO + U approach, assuming $U_{\rm eff} \approx 20$ eV. The strong interaction $U_{\rm eff}$ shifts the occupied Ce 4f bands far below the conduction band and eliminates the hybridization between the 4f and conduction band states for each $Ce_nM_mIn_{2m+3n}$ compound.

For the parent $CeIn_3$, *difference charge density* maps (figures 11(a) and 12) clearly show that electrons are accumulated near the faces of the unit cell, between the NN Ce atoms. It points to the formation of the covalent-like bondings between Ce atoms. However, the observed accumulations are not distributed exactly along the edges of the unit cell, but they are dispersed and shifted away significantly toward the midpoints of lines connecting the pairs of NN In atoms surrounding the Ce ones. This indicates the important influence of the In atoms on formation of these bondings. In effect, each Ce atom is surrounded by the 24 charge accumulations, while the lowest *valence charge density* was found near the centre of the unit cell. The comparative analysis of the *difference charge density* maps calculated for different values of the $U_{\rm eff}$ parameter applied for Ce 4f states indicates that the 4f states do not give a noticeable contribution to the charge accumulations, since these accumulations remain almost unchanged even for the very large $U_{\rm eff}$-values (∼20 eV). The hybridization between the Ce 4f and conduction band states in $CeIn_3$, observed for $U_{\rm eff}$ = 6 eV, leads only to a slight increase in charge density near the faces of the unit cell (figure 12).

Insertion of the MIn_2 layers between the $CeIn_3$ complexes results in an essential redistribution of the charge density, as presented in figure 11. First of all, it lowers the Ce point symmetry from $m3m$ in $CeIn_3$ to $4/mmm$ and $4mm$ in $CeMIn_5$ and Ce_2MIn_8 subfamilies, respectively. Consequently, it enables a change of the orbital occupied by the 4f electron from f_{xyz} in $CeIn_3$ to $f_{zx^2-zy^2}$ in $CeMIn_5$ and Ce_2MIn_8 subfamilies. Both these atomic orbitals have the same shape, but the f_{xyz} has lobes directed toward the centre of the unit cell, while the lobes of the $f_{zx^2-zy^2}$ are distributed along the lateral faces of the unit cell.

Let us consider in detail the $CeMIn_5$ compounds first. The insertion of the MIn_2 layer between each two $CeIn_3$ complexes leads to (i) an essential increase in the charge accumulations distributed between the NN Ce and In atoms; (ii) creation of significant charge accumulations near the M atoms, along the lateral faces of the unit cell.

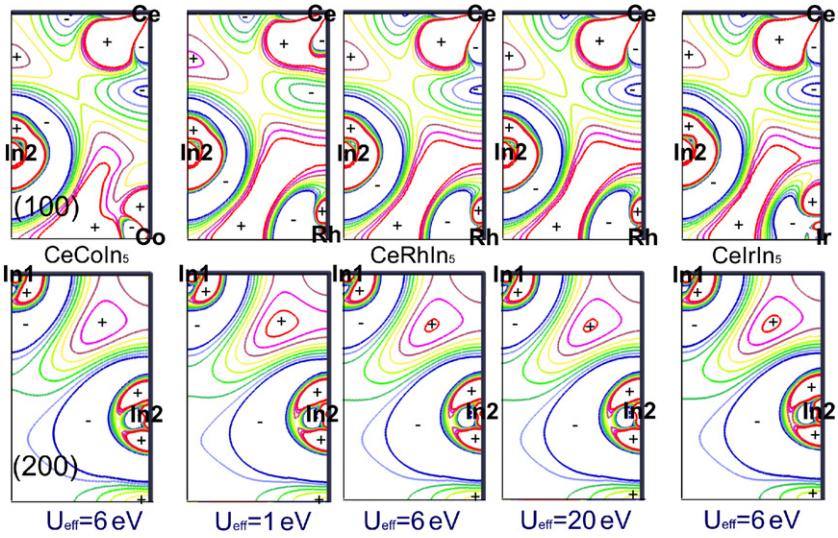

Figure 13. The difference charge densities (electron au^{-3}) for planes (100) and (200) of $CeMIn_5$ compounds calculated by the LAPW method within the GGA + SO + U approximation. For a detailed description and legend see figure 12 (colour online).

The first observation, that the charge accumulations located between the NN Ce and In atoms increase, indicates that there is considerable enhancement of *horizontal bondings* within $CeIn_3$ layers in all $CeMIn_5$ compounds in comparison with the parent $CeIn_3$ system. This effect may be responsible for the contraction of the lattice parameter a and, to some extent, also for the shortening of the $CeIn_3$-complex height, as a result of the contraction of distances between atoms contributing to these bondings.

The second effect can be related to formation of other bondings. It should be noted that the charge accumulations near the M atoms are substantially elongated toward the midpoints of lines connecting the pairs of NN In atoms surrounding the Ce ones and appear instead of the vertical bondings in parent $CeIn_3$ system. This suggests that the bondings are created between the M atom and its neighbours, Ce and In atoms. Formation of these *vertical bondings* and strengthening of bondings within the $CeIn_3$ layers result in the significant shrinking of the $CeIn_3$-complex height for all $CeMIn_5$ materials (table 2) with respect to the basic $CeIn_3$ compound.

To get insight into the role of Ce 4f electrons in bonding we have calculated *difference charge density* plots based on the band structure calculations for the $CeMIn_5$ series with different values of the U_{eff} parameter applied for Ce 4f states. Figure 13 presents the selected result for $CeRhIn_5$. Comparison of the density maps obtained for $U_{\mathrm{eff}} = 6$ eV and $U_{\mathrm{eff}} = 20$ eV shows that for the U_{eff}-value typical for Ce^{3+} there is a noticeable contribution of the Ce 4f density in interatomic regions near the lateral faces of the unit cell between the neighbouring Ce, In2 and M atoms. This suggests that the 4f electrons contribute to bonding in $CeRhIn_5$ and it is consistent with our band structure results, which points to the hybridization of the 4f states with M d and In2 p orbitals (see the discussion in section 4.3). There is no apparent direct participation of the 4f electrons in the main horizontal and vertical charge accumulations. In contrast, for $U_{\mathrm{eff}} = 1$ eV, which gives the

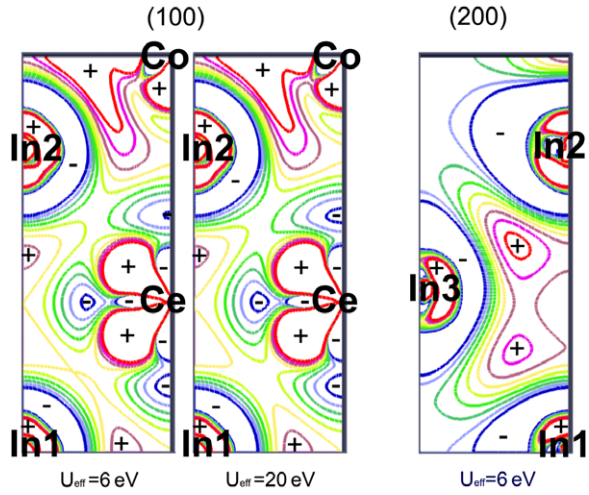

Figure 14. The difference charge densities (electron au^{-3}) for planes (100) and (200) of Ce_2CoIn_8 calculated by the LAPW method within the GGA + SO + U approximation. For a detailed description and legend see figure 12 (colour online).

best agreement between the theoretical and experimental Ce magnetic moments, the strong hybridization close to the Fermi level between the 4f and conduction band states leads to the distinct strengthening of the horizontal charge accumulations as well as to the significant increase of the *valence charge density* in the interatomic regions near the Ce atoms (figure 13). Similar results were obtained for all $CeMIn_5$ systems.

Within the $CeMIn_5$ series, the electronic charge accumulated within the horizontal bondings slightly increases with atomic number of the M atom. There are also slight changes in shape of these bondings, which can be associated with differences in the $a/h_{\mathrm{CeIn_3}}$ ratio, i.e. higher value of the ratio results in charge accumulated closer to the basal planes of the unit cell (figure 13). Simultaneously, there is also a considerable variation in vertical charge accumulations located near

Table 6. The table presents the distances between the plane passing through Ce atoms, parallel to the basal plane of the unit cell, and parallel planes crossing through In2 atoms, d_{Ce-In2}; In3 atoms, d_{Ce-In3}; M atoms, d_{Ce-M}; NN Ce atoms, d_{Ce-Ce}, for all $Ce_nM_mIn_{2m+3n}$ compounds.

Compound	d_{Ce-In2} (Å)	d_{Ce-In3} (Å)	d_{Ce-M} (Å)	d_{Ce-Ce} (Å)
$CeIn_3$	2.343	—	—	4.687
Ce_2CoIn_8	2.335	0.175	3.804	4.643
Ce_2RhIn_8	2.297	0.017	3.746	4.727
Ce_2IrIn_8	2.269	0.005	3.722	4.732
$CeCoIn_5$	2.340	—	3.770	7.540
$CeRhIn_5$	2.307	—	3.771	7.542
$CeIrIn_5$	2.289	—	3.751	7.501

the M atoms. One can expect that changes in both the vertical and the horizontal charge accumulations, resulting from the replacement of the smaller M atoms by the larger ones, are the reason for the displacement of Ce atoms toward the planes passing through the M atoms and for the shift of In2 atoms toward the basal Ce plane (table 6). In turn the shift of In2 atoms toward the basal planes of the unit cell, in the vicinity of the Ce and In1 atoms, is supposed to result in the observed elongation of the lattice parameter a within the $CeMIn_5$ subfamily of compounds. Comparison of the *difference charge density* maps calculated for $CeMIn_5$ compounds with values of U_{eff} typical for Ce^{3+} indicates that there are slightly more electrons assembled in the interatomic regions between the NN Ce, M and In2 atoms, with respect to the superposition of free atom densities, for $CeRhIn_5$ than for $CeCoIn_5$ and $CeIrIn_5$. Since the Ce 4f electrons contribute to the charge density in these regions, the effect discussed above might explain the variation in hybridization energy Δ within the $CeMIn_5$ subfamily (see the discussion in section 4.1). However, the effect is small and the precise understanding of the mechanism leading to the changes in hybridization strength (Δ) for these compounds needs further theoretical and experimental investigations.

Analogous mechanisms can be observed within the Ce_2MIn_8 subfamily. For these compounds, the charge accumulations near the M atoms are similar to that in the $CeMIn_5$ series and may also contribute to the reduction of the distance between M and its neighbouring Ce atoms. Within the Ce_2MIn_8 series, replacement of the smaller M atoms by the larger ones results in a shift of Ce atoms toward the planes crossing through M atoms and displacement of In2 atoms toward the Ce plane parallel to the basal plane of the unit cell (table 6). Both these effects, analogously as in the $CeMIn_5$ series, may be responsible for the observed elongation of the lattice parameter a as one goes from Ce_2CoIn_8 to Ce_2RhIn_8 and Ce_2IrIn_8 (table 2). The similarity between the two subfamilies discussed above is also reflected in the changes in complex of the pd bands, which are similar within both subfamilies, as proved by the XPS measurements and band structure calculations (see section 3).

However, for the Ce_2MIn_8 compounds there is also an essential redistribution of the valence charge density within the $(CeIn_3)_2$ bicomplexes relative to that in both the parent $CeIn_3$ compound and the $CeMIn_5$ systems. As demonstrated by the *difference charge density* maps for Ce_2CoIn_8 (figure 14), the insertion of the MIn_2 layers between the $(CeIn_3)_2$ bicomplexes results in the significant enhancement of charge accumulations spaced along the z-axis between the NN Ce atoms. This suggests that there is a strengthening of the vertical bondings between these Ce atoms, which may be responsible for the shrinking of the distance between these atoms in all Ce_2MIn_8 compounds relative to that in the parent $CeIn_3$ compound (table 6).

In $CeIn_3$ and $CeMIn_5$ compounds the charge accumulations parallel to the basal plane, between the Ce atoms, are symmetrical relative to the horizontal Ce planes. In the Ce_2MIn_8 series this symmetry is destroyed. The accumulations shifted toward the MIn_2 layers increased, essentially assembling more electrons, while those which are displaced in the direction of the centre of the $(CeIn_3)_2$ bicomplexes are strongly reduced, so that only their traces are visible for the Ce_2MIn_8 compounds (figures 12(b) and (c)). The observed asymmetry in horizontal bondings within the $(CeIn_3)_2$-complexes is responsible for the shift of In3 atoms, located originally within the Ce plane, towards the NN MIn_2 layers in all Ce_2MIn_8 compounds (table 6).

Two distances contribute to the c lattice parameter of the Ce_2MIn_8 unit cell. The first one is the distance between Ce and M planes parallel to the basal ones (d_{Ce-M}). The second one is the distance between Ce planes parallel to the basal ones (d_{Ce-Ce}). The changes of these distances within the Ce_2MIn_8 series are in opposite directions. d_{Ce-M} becomes smaller when the atomic number of M atoms decreases. The origin of these changes is the same as in $CeMIn_5$ compounds. The increase in the d_{Ce-Ce} value with increasing atomic number of M atoms can be explained as due to the weakening of the direct Ce–Ce bonding along the z-axis. The variation in the lattice parameter c within the Ce_2MIn_8 series results from the competition between changes in both distances. The observed changes of relative position of In3 atoms with respect to Ce planes parallel to the basal ones can also be explained in terms of the discussed mechanisms.

The comparative analysis of the *difference charge density maps* calculated for Ce_2MIn_8 series with different values of the U_{eff} parameter applied for Ce 4f states (figure 14) indicates that there is no apparent participation of the 4f electrons in the main horizontal and vertical charge accumulations. However, for $U_{eff} \approx 6$ eV the hybridization between the 4f and conduction band states leads to a slight increase in charge density near the lateral faces of the unit cell, between the NN Ce and In1 atoms as well as between the NN Ce, In2 and Co atoms. Similar results were found for all Ce_2MIn_8 compounds. This indicates that 4f electrons participate in bonding in the Ce_2MIn_8 series and it is consistent with our band structure results, which revealed that there is hybridization of the 4f states with M d states and with p states of In1 and In2 (see discussion in section 4.3).

The characteristic effect which can be observed on *valence charge density* maps for both $CeMIn_5$ and Ce_2MIn_8 subfamilies (not presented in the paper) is the growth of the region of low charge density located in the centre of the MIn_2 layers for increasing atomic number of M atoms.

Simultaneously, there is also a considerable increase in *valence charge density*, relative to the superposition of atomic densities, on the lateral faces of the unit cell, between the NN M atoms. This suggests that there are essential interactions between the NN M atoms, which might result in changes in M d bands within the $CeMIn_5$ series of compounds (see the discussion in section 4.3).

5. Concluding remarks

The electronic structure of the $Ce_nM_mIn_{2m+3n}$ compounds was investigated by the XPS measurements and *ab initio* band structure calculations. The most interesting part of our studies involved the nature of the Ce 4f states in these materials. Based on the Ce 3d XPS spectra we have found that the hybridization energy Δ between 4f and conduction electron states is rather strong for $CeMIn_5$ and Ce_2MIn_8 compounds ($\Delta \sim 90$ meV). The hybridization is slightly stronger for systems with Co and Ir than for their AF counterparts with Rh, which points to the more delocalized character of Ce 4f states in the non-magnetic compounds. The XPS valence band spectra do not give unique information about the character of 4f states in these materials. However, in the case of $CeIn_3$ we have identified the Ce 4f contribution to the XPS valence band spectrum at the binding energy of 2.1 eV. This outcome is supported by the magnetic moment analysis performed theoretically, suggesting that the character of the f states in $CeIn_3$ is rather localized, whereas for other AF compounds, $CeRhIn_5$ and Ce_2RhIn_8, a good agreement between the theoretical and experimental magnetic moments was found, also assuming that the Ce 4f states are on the border of localization. In this respect the computational results agree with the Ce 3d XPS spectrum analysis, which has shown significantly higher Δ-values for the $CeMIn_5$ and the Ce_2MIn_8 compounds than for the parent $CeIn_3$.

The study of the *valence charge density* distribution performed for all investigated compounds gives the following explanation of the properties discussed above. For all $CeMIn_5$ and Ce_2MIn_8 compounds, the increase in hybridization energy Δ, relative to that in $CeIn_3$, results from the rebuilding of the electronic charge density. Inclusion of M atoms leads to (i) formation of covalent-like bondings between Ce and M atoms, influenced by the NN In atoms, and (ii) strengthening of covalent-like bondings within the $CeIn_3$ complexes.

The variation in hybridization strength Δ within the $CeMIn_5$ subfamily can be related to the changes in *valence charge density* in interatomic regions between the NN Ce, M and In2 atoms, where the noticeable Ce 4f charge density occurs due to the hybridization with M d and In2 p states. However, the observed effect is small.

Within the Ce_2MIn_8 subfamily we have found changes in charge accumulations between the neighbouring Ce, M and In2 atoms similar to that observed for the $CeMIn_5$ compounds. This similarity between the two subfamilies is reflected also in the similar changes in the complex of pd bands formed by the hybridized p and d states of neighbouring M and In atoms. This effect is proved by both the XPS measurements and band structure calculations. It follows that the main mechanism responsible for the changes in valence band states within the Ce_2MIn_8 series should be the same as within the $CeMIn_5$ series. However, for the Ce_2MIn_8 compounds there is also an essential redistribution of the *valence charge density* within the $(CeIn_3)_2$ bicomplexes relative to that in both the parent $CeIn_3$ compound and the $CeMIn_5$ systems, which influences the Ce 4f states. Our results indicate that the variation in hybridization strength Δ within the Ce_2MIn_8 subfamily results mainly from the changes in *valence charge density* near the lateral faces of the unit cell, since there is noticeable Ce 4f electron density in these regions due to the hybridization between Ce 4f, M d, In1 p and In2 p states.

The presented results support the common picture that in the HF f electron systems the transition to the HF liquid state or the appearance of SC state is connected with delocalization of the f states due to the hybridization, as suggested previously [64]. The precise understanding of the mechanism leading to the changes in hybridization strength (Δ) and the ground state properties within the $Ce_nM_mIn_{2m+3n}$ family of compounds needs, however, further theoretical and experimental investigation.

Acknowledgments

The authors thank the Ministry of Science and Higher Education for financial support from project No 1 P03B 052 28 and for grant No N202 010 32/0487.

References

[1] Doradziński R and Spałek J 1997 *Phys. Rev.* B **56** 14239
Doradziński R and Spałek J 1998 *Phys. Rev.* B **58** 3293
For brief review see Spałek J and Doradziński R 1999 *Acta Phys. Pol.* A **96** 677
Spałek J and Doradziński R 2000 *Acta Phys. Pol.* A **97** 71
[2] Doniach S 1977 *Physica* B **91** 231
Doniach S 1977 *Valence Instability and Related Narrow Band Phenomena* ed R D Parks (New York: Plenum)
[3] Mathur N D, Grosche F M, Julian S R, Walker I R, Freye D M, Haselwimmer R K W and Lonzarich G G 1998 *Nature* **294** 39
[4] Grosche F M, Steiner M J, Agarwal P, Walker I R, Freye D M, Julian S R and Lonzarich G G 2001 *J. Phys.: Condens. Matter* **13** 2845
[5] Kawasaki S *et al* 2001 *Phys. Rev.* B **65** 020504(R)
[6] Hegger H, Petrovic C, Moshopoulou E G, Hundley M F, Sarrao J L, Fisk Z and Thompson J D 2000 *Phys. Rev. Lett.* **84** 4986
[7] Thompson J D *et al* 2001 *J. Magn. Magn. Matter.* **226** 5
[8] Fisher R A, Bouquet F, Phillips N E, Hundley M F, Pagliuso P G, Sarrao J L, Fisk Z and Thompson J D 2002 *Phys. Rev.* B **65** 224509
[9] Mito T, Kawasaki S, Zheng G-q, Kawasaki Y, Ishida K, Kitaoka Y, Aoki D, Haga Y and Onuki Y 2001 *Phys. Rev.* B **63** 220507(R)
[10] Petrovic C, Movshovich R, Jaime M, Pagliuso P G, Hundley M F, Sarrao J L, Fisk Z and Thompson J D 2001 *Europhys. Lett.* **53** 354
[11] Petrovic C, Pagliuso P G, Hundley M F, Movshovich R, Sarrao J L, Thompson J D and Fisk Z 2001 *J. Phys.: Condens. Matter* **13** L337
[12] Chen G, Ohara S, Hedo M, Uwatoko Y, Saito K, Sorai M and Sakamoto I 2002 *J. Phys. Soc. Japan* **71** 2836
[13] Nicklas M, Sidorov V A, Borges H A, Pagliuso P G, Petrovic C, Fisk Z, Sarrao J L and Thompson J D 2003 *Phys. Rev.* B **67** 020506(R)
[14] Lawrence J M and Shapiro S M 1980 *Phys. Rev.* B **22** 4379

Benoit A, Boucherle J X, Convert P, Flouquet J, Palleau J and Schweizer J 1980 *Solid State Commun.* **34** 293
[15] Grin Y N, Yarmolyuk Y P and Gladyshevskii E I 1979 *Sov. Phys.—Crystallogr.* **24** 137
Grin Y N, Rogl P and Hiebl K 1986 *J. Less-Common Met.* **121** 497
[16] Wang J L, Zeng Z, Zheng Q Q and Lin H Q 2003 *J. Appl. Phys.* **93** 6891
[17] Kawasaki S, Yashima M, Mito T, Kawasaki Y, Zheng G-q, Kitaoka Y, Aoki D, Haga Y and Onuki Y 2005 *J. Phys.: Condens. Matter* **17** S889
[18] Moore D P, Durakiewicz T, Joyce J J, Arko A J, Morales L A, Sarrao J L, Pagliuso P G, Wills J M and Olson C G 2002 *Physica* B **312/313** 134
[19] Fujimori S *et al* 2003 *Phys. Rev.* B **67** 144507
[20] Haga Y *et al* 2001 *Phys. Rev.* B **63** 060503
[21] Alver U, Goodrich R G, Harrison N, Hall D W, Palm E C, Murphy T P, Tozer S W, Pagliuso P G, Moreno N O, Sarrao J L and Fisk Z 2001 *Phys. Rev.* B **64** 180402
[22] Shishido H *et al* 2002 *J. Phys. Soc. Japan* **71** 162
[23] Harrison N *et al* 2004 *Phys. Rev. Lett.* **93** 186405
[24] Zheng G-q, Tanabe K, Mito T, Kawasaki S, Kitaoka Y, Aoki D, Haga Y and Onuki Y 2001 *Phys. Rev. Lett.* **86** 4664
[25] Fujimori S *et al* 2006 *Phys. Rev.* B **73** 224517
[26] Gamża M, Ślebarski A and Deniszczyk J 2006 *Mater. Sci. Pol.* **24** 569
[27] Elgazzar S, Opahle I, Hayn R and Oppeneer P M 2004 *Phys. Rev.* B **69** 214510
[28] Settai R *et al* 2005 *J. Phys. Soc. Japan* **74** 11
[29] Biasini M, Ferro G and Czopnik A 2003 *Phys. Rev.* B **68** 094513
[30] Thessieu C, Ishida K, Kawasaki S, Mito T, Kawasami Y, Zheng G-q, Kitajka Y and Onuki Y 2000 *Physica* B **281/282** 9
[31] Singh D 1994 *Plane Waves, Pseudopotentials and The LAPW Method* (Dordrecht: Kluwer)
[32] Koepernik K and Eschrig H 1999 *Phys. Rev.* B **59** 1743
[33] Blaha P, Schwarz K, Madsen G, Kvasnicka D and Luitz J 2001 *Program for Calculating Crystal Properties, WIEN2k,* Vienna University of Technology (ISBN 3-9501031-1-2)
[34] Pardew J P, Burke K and Ernzerhof M 1996 *Phys. Rev. Lett.* **77** 3865
[35] Koelling D D and Harmon B N 1977 *J. Phys. C: Solid State Phys.* **10** 3107
[36] MacDonald A H, Pickett W E and Koelling D D 1980 *J. Phys. C: Solid State Phys.* **13** 2675
[37] Anisimov V I, Solovyev I V, Korotin M A, Czyżyk M R and Sawatzky G A 1993 *Phys. Rev.* B **48** 16929
Anisimov V I, Zaanen J and Andersen O K 1991 *Phys. Rev.* B **44** 943
Anisimov V I, Aryasetiawan F and Lichtenstein A I 1997 *J. Phys.: Condens. Matter* **9** 767
[38] Eschrig H, Koepernik K and Chaplygin I 2003 *J. Solid State Chem.* **176** 482
[39] Perdew J P and Wang Y 1992 *Phys. Rev.* B **45** 13244
[40] Eschrig H 1989 *Optimized LCAO Method and the Electronic Structure of Extended Systems* (Berlin: Springer)
[41] Yeh J J and Lindau J 1985 *At. Data Nucl. Data Tables* **32** 1
[42] Kim J S, Alwood J, Stewart G R, Sarrao J L and Thompson J D 2001 *Phys. Rev.* B **64** 134524
[43] Kalychak Ya M, Zaremba V I, Baranyak V M, Bruskov V A and Zavalij P Yu 1989 *Izv. Akad. Nauk SSSR Metally* **1** 213
[44] Macaluso R T, Sarrao J L, Moreno N O, Pagliuso P G, Thompson J D, Fronczek F R, Hundley M F, Malinowski A and Chan J Y 2003 *Chem. Mater.* **15** 1394
[45] Moshopoulou E G, Sarrao J L, Pagliuso P G, Moreno N O, Thompson J D, Fisk Z and Ibberson R M 2002 *Appl. Phys.* A **74** 895
[46] Baer Y, Bush G and Cohn P 1975 *Rev. Sci. Instrum.* **46** 466
[47] Tougaard S and Sigmund P 1982 *Phys. Rev.* B **25** 4452
[48] Fuggle J C, Campagna M, Zolnierek Z, Lässer R and Platau A 1980 *Phys. Rev. Lett.* **45** 1597
[49] Fuggle J C, Hillebrecht F U, Zolnierek Z, Lässer R, Freiburg Ch, Gunnarsson O and Schönhammer K 1983 *Phys. Rev.* B **27** 7330
[50] Ślebarski A, Zawada T, Spałek J and Jezierski A 2004 *Phys. Rev.* B **70** 235112
[51] Seah M P and Dench W A 1979 *Surf. Interface Anal.* **1** 2 and references there
[52] Wuilloud E, Moser H R, Schneider W-D and Baer Y 1983 *Phys. Rev.* B **28** 7354 (Rapid Communications)
[53] Fuggle J C, Gunnarsson O, Sawatzky G A and Schönhammer K 1988 *Phys. Rev.* B **37** 1103
[54] Lawrence J 1979 *Phys. Rev.* B **20** 3770
[55] Gunnarsson O and Schönhammer K 1983 *Phys. Rev.* B **28** 4315
[56] Doniach S and Šunjić M 1970 *J. Phys. C: Solid State Phys.* **3** 286
[57] Kim H-D, Tjernberg O, Chiaia G, Kumigashira H, Takahashi T, Duó L, Sakai O, Kasaya M and Lindau I 1997 *Phys. Rev.* B **56** 1620
[58] Raj S, Iida Y, Souma S, Sato T, Takahashi T, Ding H, Ohara S, Hayakawa T, Chen G F, Sakamoto I and Harima H 2005 *Phys. Rev.* B **71** 224516
[59] Baer Y, Ott H R, Fuggle J C and De Long L E 1981 *Phys. Rev.* B **24** 5384
Lang J K, Baer Y and Cox P A 1981 *J. Phys.* F **11** 121
Herbst J F, Watson R E and Wilkins J W 1978 *Phys. Rev.* B **17** 3089
Herbst J F and Wilkins J W 1979 *Phys. Rev. Lett.* **43** 1760
Anisimov V I and Gunnarsson O 1991 *Phys. Rev.* B **43** 7570
[60] Loewenhaupt M and Fischer K H 1993 *Handbook of the Physics and Chemistry of Rare Earths* vol 16, ed K A Gschneidner Jr and L R Eyring (Amsterdam: North-Holland) p 1
[61] Bao W, Pagliuso P G, Sarrao J L, Thompson J D, Fisk Z, Lynn J W and Erwin R W 2000 *Phys. Rev.* B **62** R14621
[62] Bao W, Pagliuso P G, Sarrao J L, Thompson J D, Fisk Z and Lynn J W 2001 *Phys. Rev.* B **64** 020401(R)
[63] Bao W, Aeppli G, Christianson A D, Fisk Z, Hundley M F, Lacerda A H, Lynn W, Pagliuso P G, Sarrao J L and Thompson J D 2002 *Int. J. Mod. Phys.* B **16** 3244
[64] Grewe N and Steglich F 1991 *Handbook of the Physics and Chemistry of Rare Earths* vol 14, ed K A Gschneidner Jr and L R Eyring (Amsterdam: North-Holland) p 343
[65] Moreno N O, Hundley M F, Pagliuso P G, Movshovich R, Nicklas M, Thompson J D, Sarrao J L and Fisk Z 2002 *Physica* B **312/313** 274